

2D Titanium carbide printed flexible ultra-wideband monopole antenna for wireless communications

Received: 30 June 2022

Accepted: 30 November 2022

Published online: 17 January 2023

Check for updates

Weiwei Zhao^{1,5}, Hao Ni^{2,5}, Chengbo Ding¹, Leilei Liu²✉, Qingfeng Fu², Feifei Lin¹, Feng Tian³, Pin Yang¹, Shujuan Liu¹, Wenjun He¹, Xiaoming Wang¹, Wei Huang^{1,4}✉ & Qiang Zhao^{1,2}✉

Flexible titanium carbide (Ti_3C_2) antenna offers a breakthrough in the penetration of information communications for the spread of Internet of Things (IoT) applications. Current configurations are constrained to multi-layer complicated designs due to the limited conformal integration of the dielectric substrate and additive-free Ti_3C_2 inks. Here, we report the flexible ultrawideband Ti_3C_2 monopole antenna by combining strategies of interfacial modification and advanced extrusion printing technology. The polydopamine, as molecular glue nano-binder, contributes the tight adhesion interactions between Ti_3C_2 film and commercial circuit boards for high spatial uniformity and mechanical flexibility. The bandwidth and center frequency of Ti_3C_2 antenna can be well maintained and the gain differences fluctuate within ± 0.2 dBi at the low frequency range after the bent antenna returns to the flat state, which conquers the traditional inelastic Cu antenna. It also achieves the demo instance for the fluent and stable real-time wireless transmission in bending states.

The advancement of the Internet of Things (IoT) system greatly demands the seamless integration of radio-frequency (RF) antennas and circuits at wide frequency band for device-device communication^{1,2}. Ultrathin and flexible antenna components have arisen a great interest towards reliable wireless connectivity with miniaturized and wearable electronics, including sensors, displays, data processing devices, etc³. The key materials are expected to be flexible with high electrical conductivity and tolerable mechanical deformation⁴. In comparison with conventionally used metals⁵, carbon-based nanomaterials⁶, and polymers⁷, two-dimensional titanium carbide (Ti_3C_2) is becoming nominated star materials for RF

antennas due to its intrinsic high electrical conductivity ($10,000\text{--}20,000\text{ S cm}^{-1}$), good skin depth (2.4 GHz, $10\ \mu\text{m}$), excellent mechanical strength and easy processibility^{8–11}. For example, in 2016, Gogotsi et al. first explored the potential applications of Ti_3C_2 nanomaterials in the flexible dipole antennas in the WiFi frequency band (2.4 GHz)⁸. In their later work, a breakthrough shows that $5.5\ \mu\text{m}$ -thick Ti_3C_2 patch antenna has a comparable radiation efficiency ($>99\%$) at 16.4 GHz, which is almost comparable with that of a standard $35\ \mu\text{m}$ -thick copper patch antenna. It makes Ti_3C_2 promising for integrated RF communications in flexible and wearable IoT devices. However, two major challenges remain on the construction of Ti_3C_2 antenna. On the

¹State Key Laboratory of Organic Electronics and Information Displays & Jiangsu Key Laboratory for Biosensors, Institute of Advanced Materials (IAM), Nanjing University of Posts & Telecommunications, 9 Wenyuan, Nanjing 210023, P. R. China. ²College of Electronic and Optical Engineering & College of Flexible Electronics (Future Technology), National and Local Joint Engineering Laboratory of RF Integration and Micro-Assembly Technology, Nanjing University of Posts & Telecommunications, 9 Wenyuan, Nanjing 210023, P. R. China. ³Key Lab of Broadband Wireless Communication and Sensor Network Technology, Nanjing University of Posts and Telecommunications, 9 Wenyuan, Nanjing 210023, P. R. China. ⁴Frontiers Science Center for Flexible Electronics (FSCFE), MIIT Key Laboratory of Flexible Electronics (KLoFE), Northwestern Polytechnical University, Xi'an 710072, P. R. China. ⁵These authors contributed equally: Weiwei Zhao, Hao Ni. ✉ e-mail: liull@njupt.edu.cn; provost@nwpu.edu.cn; iamqzhao@njupt.edu.cn

one hand, the utilization of polyethylene terephthalate (PET) and double-sided tape between Ti_3C_2 layer and commercial circuit boards causes the sophisticated manufacturing process as well as hinders the direct conformal integration with flexible electronics and chips, thus leading to unsatisfactory power delivery and sensitive resonant frequency in wireless communication¹². On the other hand, the working bandwidth is relatively narrow, and it is difficult to meet the ultrawideband requirements. Hence, it is necessary to exploit flexible ultrawideband Ti_3C_2 monopole antennas fabricated through the progressive microfabrication technique.

As one of the representative direct ink printing protocols, the extrusion printing technique has been a revolutionary and eco-friendly manufacturing route for the mass production of flexible integrated electronics with high-resolution geometry patterns and digital customization^{13–15}. It not only can generally deposit the functional viscoelastic inks with a large concentration window and suitable fluidic properties (e.g., surface tension and viscosity) under ambient conditions^{16–18}, but also has apparent advantages in realizing high-precision conformal printing on different substrates (whether flat or curved) without additional masks and accessories, as well as avoiding time-consuming and complicated transfer processes, which is superior to previously reported screen printing, physical vapor deposition, and spray coating, etc.^{2,19–21}. Substantial progresses demonstrate that additive-free Ti_3C_2 inks have inherent properties, including excellent dispersion quality, negative surface charge, and hydrophilicity¹³. Accordingly, they are proved to be particularly suitable for printing electronics, including transparent electrodes²², transistors²³, photodetectors²⁴, energy storage devices²⁵, and sensors²⁶. It provides a paradigm for the construction of patch antennas with highly compact

and intricately shaped components. However, as a core component, the commercial dielectric substrate is short of interfacial adhesion with active functional materials caused by chemically inert, smooth, and hydrophobic surface⁶. Thus, it is also highly desirable to combine the interface optimization process and extrusion printing technology for manufacturing flexible ultrawideband Ti_3C_2 monopole antennas capable of compact integration.

Here, we report the direct extrusion printing technology of additive-free concentrated Ti_3C_2 inks for flexible ultrawideband Ti_3C_2 monopole antenna. The polydopamine (PDA) is chosen as a molecular glue nano-binder between Ti_3C_2 film and dielectric substrate, contributing to the conformal integrated microstrip transmission lines (TLs) and antennas with high spatial uniformity and mechanical flexibility. The reflection coefficient S_{11} and gain of Ti_3C_2 antenna can be well maintained after cyclic bending. The demonstration of wireless movie transmission in bending states is well achieved through the wireless communication platform.

Results

Extrusion printing for flexible ultrawideband Ti_3C_2 monopole antenna

The multi-layered (m-) Ti_3C_2 is synthesized by selective removal of the aluminum layer from the commercial Ti_3AlC_2 phase (Fig. 1a and Supplementary Fig. 1). Delaminated Ti_3C_2 is prepared through bath sonication. The abundant negative electrostatic charges (e.g., -F, -OH, and -O) on the hydrophilic Ti_3C_2 nanosheets lead to stable aqueous inks (Supplementary Fig. 1c). The concentrated viscous Ti_3C_2 inks can be directly extrusion-printed for flexible patterned patch antenna (Fig. 1b and Supplementary Fig. 2). The printing technique is also

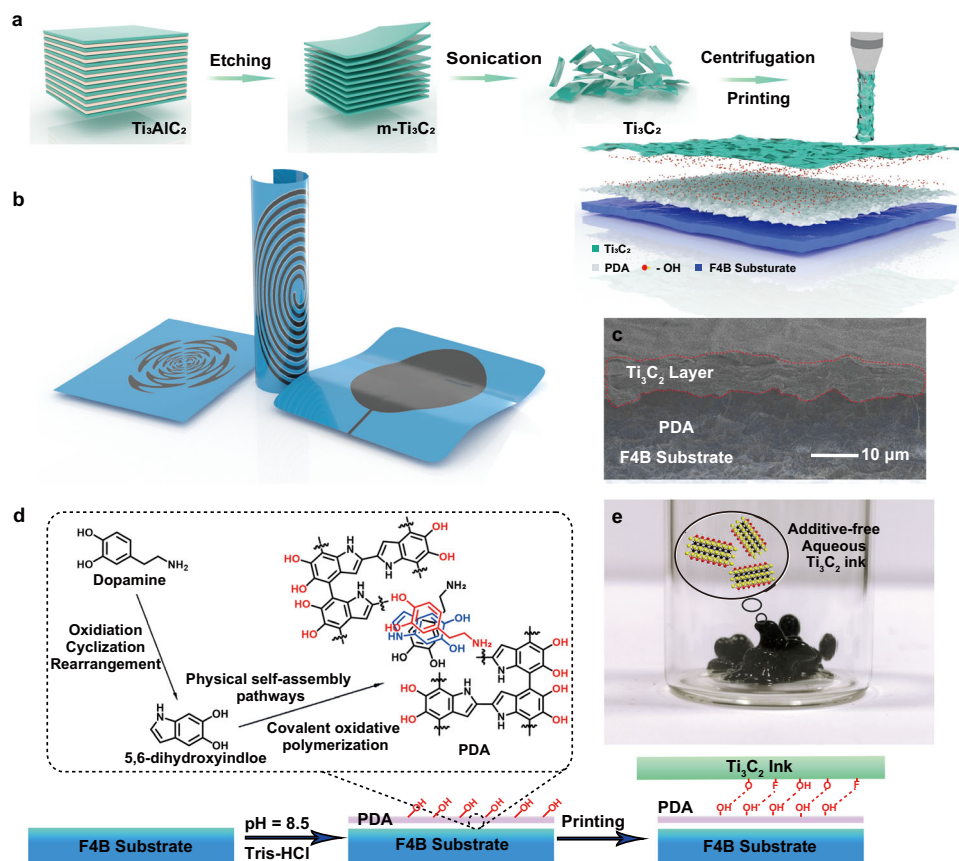


Fig. 1 | Preparation of Ti_3C_2 for antenna. **a** The schematic pathways for ultrathin Ti_3C_2 nanosheets and the direct extrusion printing of Ti_3C_2 inks for flexible antennas. **b** Different patterns of flexible Ti_3C_2 antennas. **c** The cross-sectional SEM

image of Ti_3C_2 antennas including Ti_3C_2 layer, polydopamine (PDA) and F4B220M (F4B) substrate. **d** Schematic illustration of preparation process for Ti_3C_2 antennas. **e** The optical photograph of Ti_3C_2 inks.

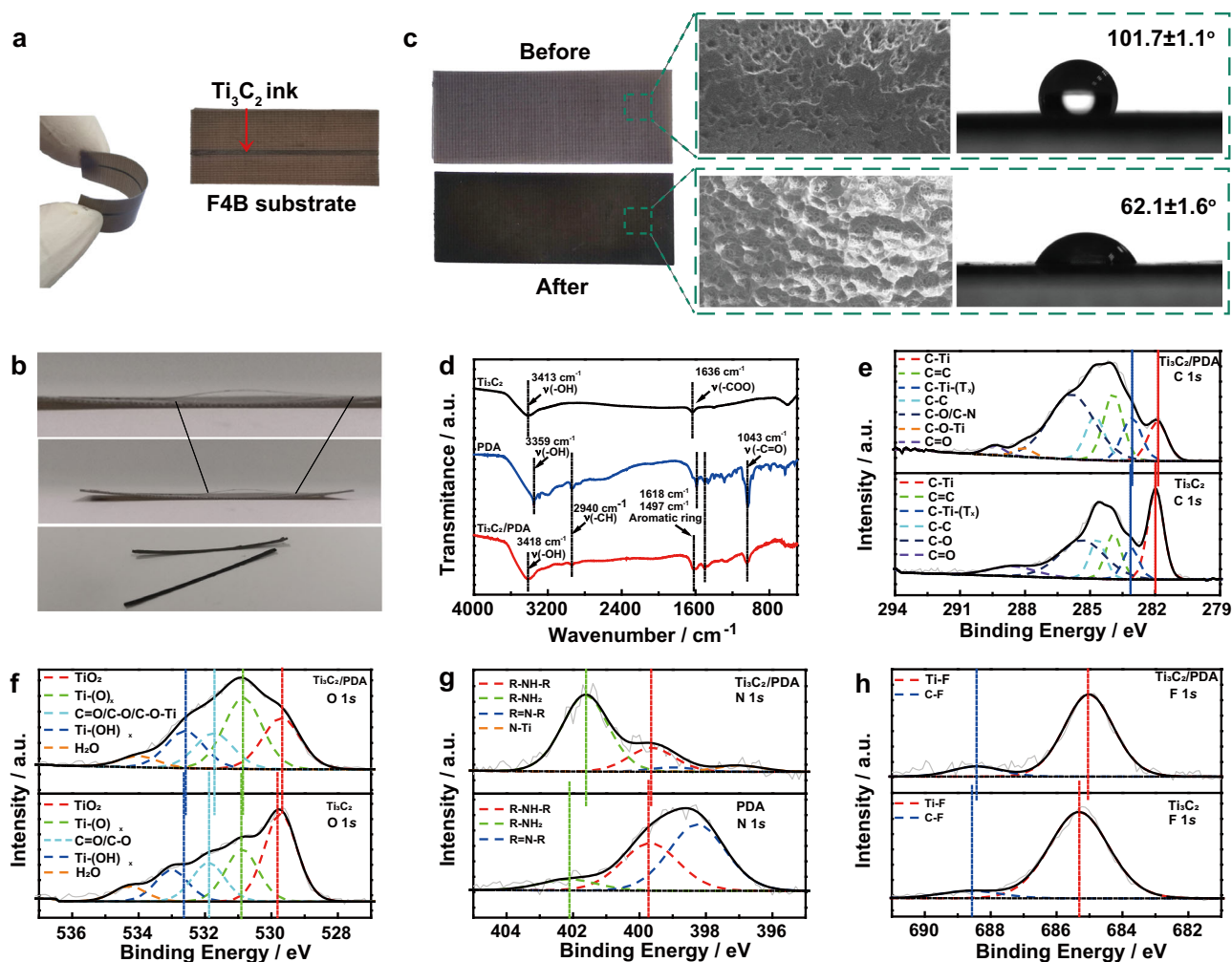


Fig. 2 | Characterization of Ti_3C_2 microstrip transmission lines (TLs). **a** Digital images of flat and bent Ti_3C_2 microstrip TLs with PDA coating. **b** Digital images of Ti_3C_2 microstrip TLs without PDA coating and the exfoliated Ti_3C_2 layer. **c** Digital

image, SEM image, and contact angle of F4B dielectric substrate before and after PDA depositing. **d** FT-IR spectra of Ti_3C_2 , PDA and $\text{Ti}_3\text{C}_2/\text{PDA}$. **e** XPS C 1s, **f** XPS O 1s, **g** XPS N 1s, and **h** XPS F 1s of $\text{Ti}_3\text{C}_2/\text{PDA}$, Ti_3C_2 or PDA.

precise for complicated flexible electronic circuits (Fig. 1b and Supplementary Fig. 3). The interconnected multilayer Ti_3C_2 film can be uniformly coated on PDA-modified commercial polytetrafluoroethylene dielectric substrate (The model is F4B220M. It is abbreviated as F4B substrate in this work) (Fig. 1c and Supplementary Fig. 4). Concretely, the F4B dielectric substrate is first modified with dopamine (DA) monomers in Tris-HCl buffer solution (pH = 8.5) (Fig. 1d). Then, the self-polymerization of DA monomers occurs via the intramolecular cyclization and intermolecular polymerization²⁷. The formed PDA layer acts as a secondary platform to improve the interfacial adhesion interactions between the dielectric substrate and printed Ti_3C_2 film, contributing the conformal integrated Ti_3C_2 antennas with the high spatial uniformity and mechanical flexibility (Fig. 1e).

Flexible and compact Ti_3C_2 microstrip TLs

The rational design of TLs is vital for low transmission loss to minimize signal attenuation and distortion²⁸. To achieve the compact integration, Ti_3C_2 TL is directly extrusion-printed on the PDA-modified F4B dielectric substrate (Fig. 2a). The total thickness of different layers is lower than that of previous reports (Supplementary Table 1). The as-fabricated Ti_3C_2 microstrip TLs can be bent at a large bending angle, showing excellent mechanical stability (Fig. 2a). While, the Ti_3C_2 TL is easy to fall off from the F4B dielectric substrate in the absence of PDA coatings (Fig. 2b). It shows that PDA irreplaceably enables to enhance

the adhesion strength between Ti_3C_2 layer and F4B dielectric substrate. The surface properties of F4B dielectric substrate are systematically analyzed before and after PDA treatment (Fig. 2c). Scanning electron microscopy (SEM) images show that the surface roughness of F4B dielectric substrate increases after the uniform adhesion of PDA coatings. The contact angle of water on the F4B dielectric substrate decreases from $101.7 \pm 1.1^\circ$ to $62.1 \pm 1.6^\circ$ ²⁹. It proves that the hydrophilicity is improved due to the exposure of the hydroxyl functional groups from PDA³⁰. Fourier transform infrared (FT-IR) spectrum of $\text{Ti}_3\text{C}_2/\text{PDA}$ is composed of the main characteristic peaks of Ti_3C_2 and PDA (Fig. 2d). The peaks at around 1618 and 1497 cm^{-1} show obvious shifts in comparison with those of PDA and Ti_3C_2 , suggesting the interaction between catechols/quinone groups in PDA and terminal groups (-OH/-O/-F) of Ti_3C_2 ³¹. X-ray photoelectron spectroscopy (XPS) of $\text{Ti}_3\text{C}_2/\text{PDA}$ demonstrates the surface compositions of C, N, Ti, O, and F elements at around 285.0, 401.2, 456.5, 531.2, and 685.3 eV, respectively (Supplementary Fig. 5a). Compared with pristine Ti_3C_2 , $\text{Ti}_3\text{C}_2/\text{PDA}$ has a newly appeared peak at 288.0 eV in C 1s spectrum, which is assigned to the catechol-titanium coordination bond (C-O-Ti) (Fig. 2e)³². In addition, C-Ti and C-Ti-(T)_x peaks downshift towards the lower binding energy due to the electron transfer from PDA to Ti_3C_2 ³³. For O 1s spectrum of $\text{Ti}_3\text{C}_2/\text{PDA}$, the quinone state (C=O) peak possibly overlaps with C-O-Ti peak (Fig. 2f)^{34,35}. The downshift tendency for Ti-(OH)_x, Ti-(O)_x, and TiO_2 is consistent with C 1s³⁶. Ti 2p spectrum also has the similar changes (Supplementary Fig. 5b). Compared with PDA,

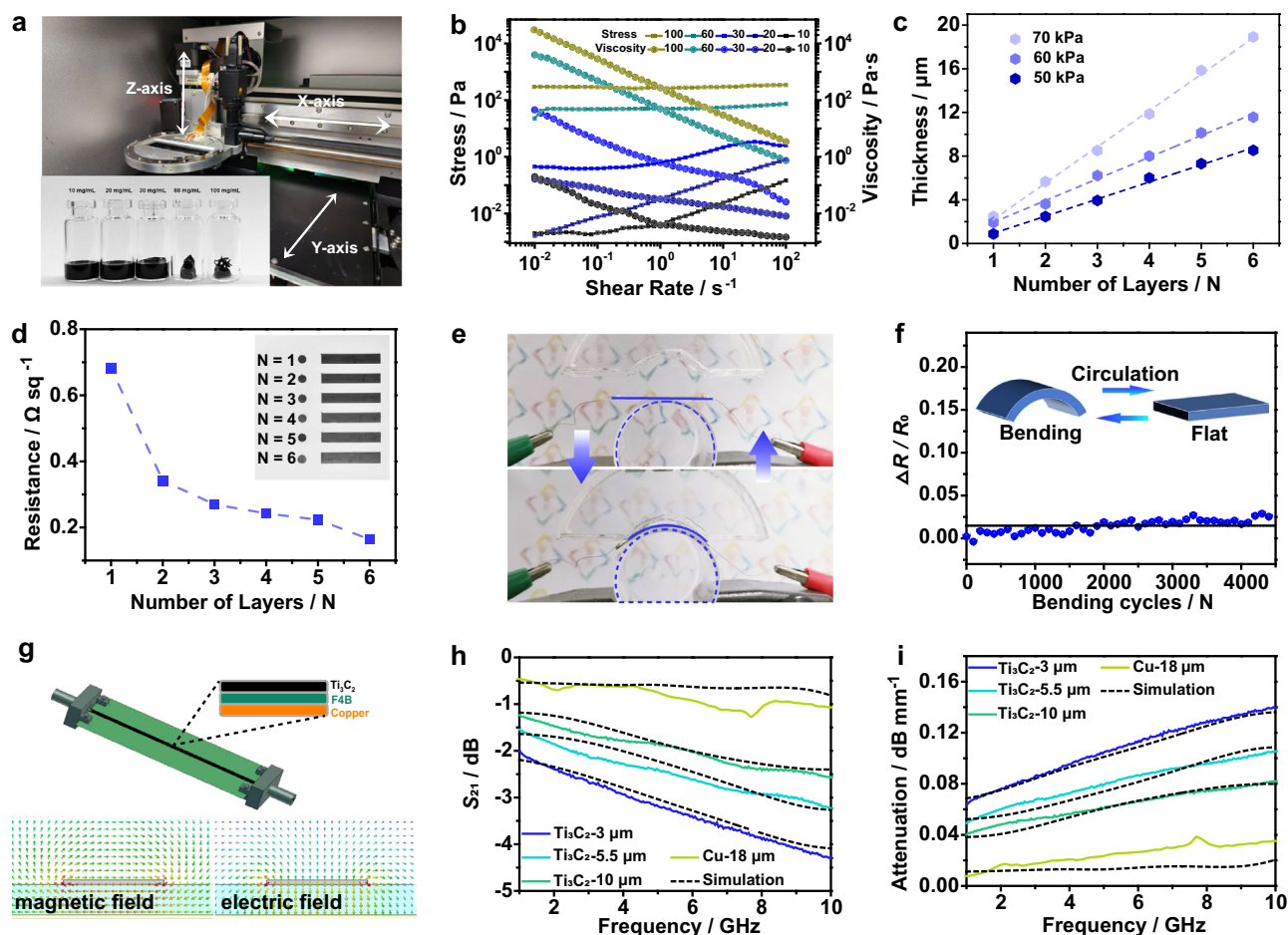


Fig. 3 | Extrusion printing for Ti_3C_2 microstrip TLs. **a** The internal structure of a microelectronic printer. Inset: Photographs of various Ti_3C_2 inks. **b** Stress and viscosity plotted as a function of shear rate. **c** Thickness plotted as a function of layer number. **d** Sheet resistance plotted as a function of layer number. Inset: Optical images of various printed lines (3 cm in length, 50 kPa) with different layer

numbers. **e** Diagram of the bending test. **f** $\Delta R/R_0$ at different bending cycles. **g** Schematic configuration of Ti_3C_2 microstrip TLs. Inset: The cross-sectional view shows the materials in different layers. Simulated electromagnetic field distribution of Ti_3C_2 TLs. Transmission coefficient S_{21} (**h**) and attenuation constant (**i**) of 3 cm-long Ti_3C_2 TLs with different thicknesses.

the lower binding energy of the primary amine (R-NH-R) and secondary amine (R = N-R) peaks is ascribed to the hydrogen bonding interactions between PDA and Ti_3C_2 (Fig. 2g)³⁷. The new N-Ti peak at 396.8 eV is assigned to the binding of amine at the unternminated Ti sites. The binding energy downshifts of F 1s (i.e., Ti-F and C-F) are mainly attributed to the hydrogen bonding with -O groups of PDA (Fig. 2h). The binding affinity and hydrogen bonding between PDA and Ti_3C_2 are the main connection modes³⁷. Therefore, PDA can act as the role of molecular glue nano-binder to reinforce the compact interaction between F4B dielectric substrate and Ti_3C_2 layer. The PDA treatment provides a universal and simple strategy to connect Ti_3C_2 materials and dielectric substrate for microstrip TLs and antennas.

Performance measurement of Ti_3C_2 microstrip TLs

In the extrusion printing, the solid-like ink is extruded as a filament through a nozzle and deposited on the substrate for a fine-resolution printing^{38,39}. The printing pass can be well adjusted by the accurate orientation of X-axis and Y-axis (Fig. 3a and Supplementary Fig. 6). The extrusive strength is controlled by atmospheric pressure. The printing height is adjusted along the Z-axis. For the Ti_3C_2 inks with different concentrations of 10, 20, 30, 60, and 100 mg mL⁻¹, the ink's viscosity increases with the raised concentrations at a constant shear rate and decreases with the increase of shear rates at a certain of concentration (Fig. 3b). It presents a clear shear-thinning behavior and non-Newtonian fluid characteristics for continuous extrusion printing

process⁴⁰. While, the stress has the contrary tendency to viscosity. In combination with the viscoelastic curves and Hershel-Bulkley fluid model, the optimal ink concentration is selected as 60 mg mL⁻¹ with the yield stress of 48 Pa, which is the most suitable parameter for the actual extrusion printing (Supplementary Figs. 7 and 8)⁴¹. By adjusting the extrusive pressure (i.e., 50, 60, and 70 kPa), the thickness measured by step profiler can be effectively adjusted (Fig. 3c and Supplementary Fig. 9). For example, the thickness gradually increases from 8.4 μm for 50 kPa to 12.1 μm for 60 kPa and 14.1 μm for 70 kPa at the layer number (N) of 6. The thickness linearly increases with the layer number at a certain pressure of 50 kPa. That is 1.2, 2.7, 3.8, 5.9, 7.7, and 8.4 μm for the layer number of 1, 2, 3, 4, 5, and 6, respectively. The sheet resistance of Ti_3C_2 film significantly decreases from 0.68 Ωsq^{-1} to 0.16 Ωsq^{-1} with 6-layer overprints (Fig. 3d). As the 3 μm -thick Ti_3C_2 TLs are periodically bent at a curvature radius of 1.5 cm (Fig. 3e), the relative resistance only has <2% change after 5,000 bending cycles, showing the excellent cyclic bending stability of Ti_3C_2 TLs (Fig. 3f).

Ti_3C_2 microstrip TLs can work through directly connecting with two pressed connectors without soldering (Fig. 3g). The simulated electromagnetic field distribution of quasi-TEM mode for Ti_3C_2 microstrip TLs agrees with that made of conventional metal²¹. Ti_3C_2 microstrip TLs with three different thicknesses (i.e., 3, 5.5, and 10 μm) are prepared and named as Ti_3C_2 -3 μm , Ti_3C_2 -5.5 μm and Ti_3C_2 -10 μm , respectively. Scattering parameters (*S*-parameter S_{11} and S_{21}) of all Ti_3C_2 microstrip TLs are measured at the frequency range from 1 to

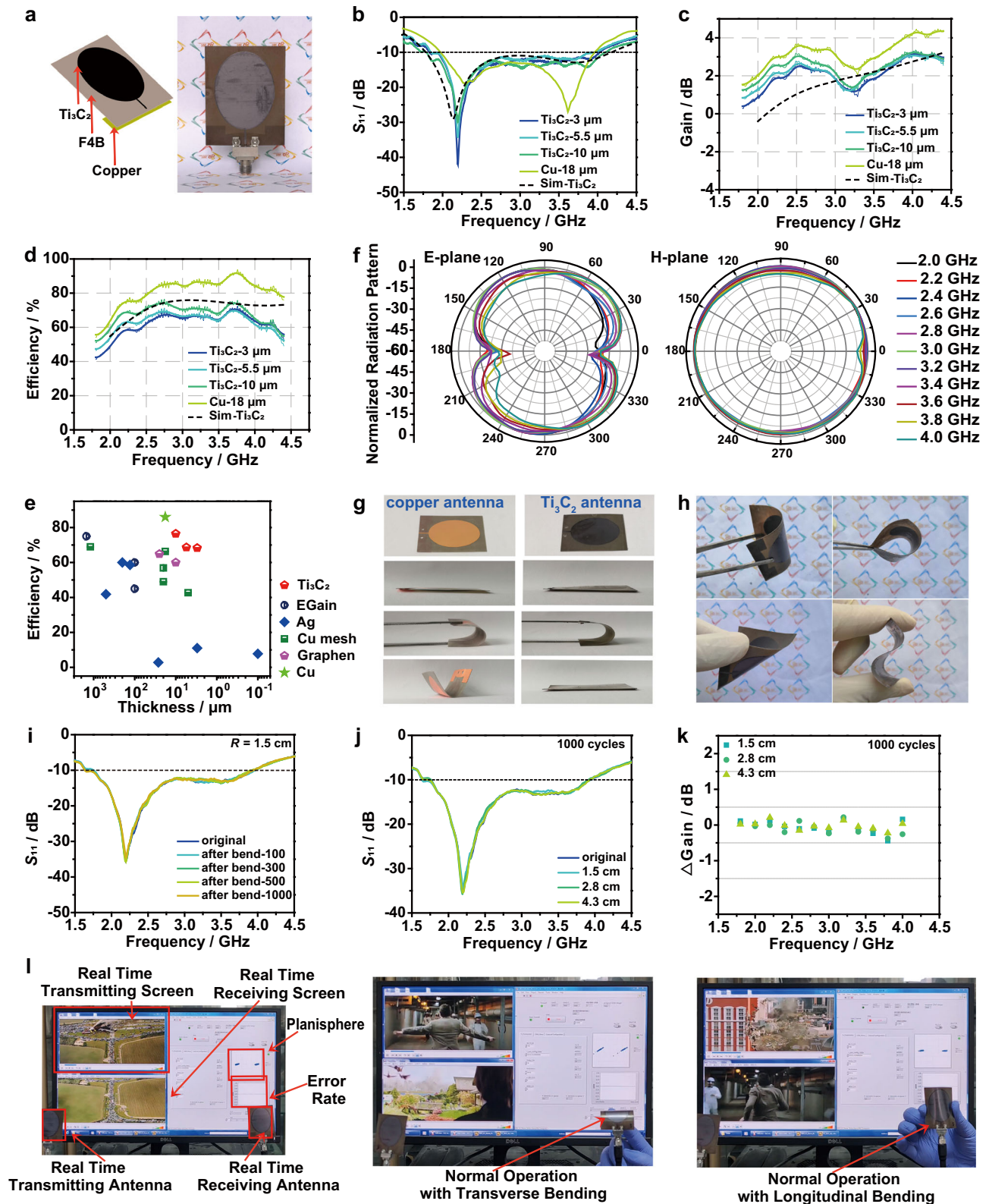


Fig. 4 | Characterization and application for ultrawideband Ti_3C_2 monopole antennas. **a** Schematic, and optical photograph of flexible Ti_3C_2 antennas on dielectric substrate with a pressed connector. **b** Measured and simulated S_{11} parameter of Ti_3C_2 antennas. Measured and simulated gain (**c**) and radiation efficiency (**d**) of Ti_3C_2 antennas. **e** A comparison of radiation efficiency versus thickness for Ti_3C_2 with metal and other materials as patch antennas. **f** Typical radiation pattern of Ti_3C_2 -5.5 μm antennas measured in the anechoic chamber. The unit is dBi.

g Digital photographs of copper antennas and Ti_3C_2 antennas. **h** Digital photographs of Ti_3C_2 antennas in various deformations. S_{11} parameter of Ti_3C_2 -5.5 μm antennas after different bending cycles at $R = 1.5$ cm (**i**) and after 1000 bending cycles under different bending radii (**j**). **k** Gain difference of Ti_3C_2 -5.5 μm antennas after 1000 bending cycles under different bending radii. **l** Demonstration of Ti_3C_2 antennas for wireless communication.

10 GHz using a vector network analyzer (Fig. 3h and Supplementary Fig. 10). The commercial 18 μm -thick copper TLs with the same geometry are manufactured as a reference. S_{11} of Ti_3C_2 microstrip TLs is kept below -10 dB (Supplementary Fig. 10). Transmission coefficient S_{21} of all TLs decreases with increasing frequencies in the range of 1–10 GHz due to the skin depth effects⁴². S_{21} also increases with the increased thickness of Ti_3C_2 microstrip TLs because of the decreased sheet resistance (Fig. 3c, d). The attenuation constant (α) of Ti_3C_2 microstrip TLs is calculated by S_{11} and S_{21} (Fig. 3i). It increases with frequency for a certain thickness and decreases with thickness from 3 to 10 μm . It is worth noting that the attenuation constant of Ti_3C_2 -10 μm microstrip TL is only 0.102 dB mm^{-1} at 2.4 GHz while that of the copper TL is 0.052 dB mm^{-1} . Even for Ti_3C_2 -3 μm TL, the attenuation constant only increases to 0.171 dB mm^{-1} . Although the attenuation constant is worse than that of 18 μm -thick copper TL, it is still acceptable to be used as a substitute for traditional metal in RF communication systems^{8,43}. The measurement of the Ti_3C_2 antenna in the later part supports this point.

Ultrawideband Ti_3C_2 monopole antenna

The simulated and measured models of the ultrawideband Ti_3C_2 monopole antennas are designed with Ti_3C_2 patch, dielectric substrate, and ground plane (Fig. 4a and Supplementary Fig. 11–12). During the test, the coaxial cable is connected through the pressure contact without soldering. Three Ti_3C_2 antennas with different thicknesses (i.e., 3, 5.5, and 10 μm), which are named as Ti_3C_2 -3 μm , Ti_3C_2 -5.5 μm and Ti_3C_2 -10 μm , respectively, are fabricated for measurements (Supplementary Fig. 13 and Supplementary Table 2). A copper antenna with the same design is used for comparison. The reflection coefficient S_{11} is lower than -10 dB in working frequency band of 1.7–4.0 GHz, indicating that the antenna can well receive the energy input by the vector network analyzer's feeder (Fig. 4b). It is well matched with the simulation results. As the thickness of Ti_3C_2 components decreases, the deeper notch of S_{11} curves appears due to stronger local resonance characteristics and decreased radiation efficiency of the antenna^{44,45}. The relative bandwidth of the Ti_3C_2 antennas reaches $75\% \pm 3\%$, covering WLAN, Bluetooth, 5G (n41, n78) frequency bands and far exceeding other Ti_3C_2 antennas at this stage^{8,21,43}. Its long-term stability lays the foundation for practical applications (Supplementary Fig. 14). The simulated current distribution of Ti_3C_2 monopole patches is identical to that of a metallic monopole antenna (Supplementary Fig. 15). The loss of Ti_3C_2 antenna is slightly higher than that of Cu antenna in high-frequency region, which makes Ti_3C_2 antennas have the lower Q value. The working bandwidth of Ti_3C_2 antennas at -10 dB is expanded and is comparable to the traditional Cu antenna²². The measured gain and total efficiency of Ti_3C_2 antenna are in the same trend as the copper antenna, which increases with the thickness due to the decreased conductor loss (Fig. 4c, d). The gain of Ti_3C_2 antenna is about 1 dBi less than that of the copper antenna, but remains at a high gain for a monopole antenna overall. It can be further increased through improving the conductivity of Ti_3C_2 component, using alternative substrate with lower dielectric loss, increasing antenna orientation, or combining multiple antennas into an antenna array^{2,46}. The radiation efficiency reaches 68.4% for Ti_3C_2 -3 μm , 68.7% for Ti_3C_2 -5.5 μm , and 76.5% for Ti_3C_2 -10 μm , which may be further increased through improving the conductivity of Ti_3C_2 layer or adopting suitable substrates with lower dielectric loss^{2,46}. The increased gain and efficiency tendency with the thickness of Ti_3C_2 patches are attributed to the decreased conductor loss⁴⁷. The radiation efficiency at 2.4 GHz of Ti_3C_2 antenna is only $14\% \pm 5\%$ lower than the copper counterpart. It is also higher than antennas made of other materials (Fig. 4e and Supplementary Table 3). The normalized radiation patterns of Ti_3C_2 antenna are consistent with the pattern of the standard monopole antenna (Fig. 4f). It is a 8 shape on E-plane and a circle on H-plane. The three-dimensional (3D) radiation patterns

obtained by the full-wave simulations software intuitively show that the Ti_3C_2 monopole antenna can radiate omnidirectionally on H-plane (Supplementary Figs. 16–18). The as-fabricated Ti_3C_2 antenna can be randomly twisted, showing excellent flexibility (Fig. 4g, h and Supplementary Movie 1). For comparison, the copper monopole antenna with the same structure has no resilience at any bending angles. The absence of PDA adhesive layer between Ti_3C_2 and F4B dielectric substrate results in structural instability (Supplementary Fig. 19). The cyclic bending tests are further performed to investigate the stability of Ti_3C_2 antenna. Typically, the Ti_3C_2 -5.5 μm antenna is first bent for 100, 300, 500, and 1000 cycles at the bending radius (R) of 1.5 cm (Fig. 4i). There is no obvious shift for bandwidth and center frequency after the antenna returns to the flat state. S_{11} values also have negligible changes after 1000 bending cycles at the bending radii of 1.5, 2.8, and 4.3 cm (Fig. 4j). The corresponding gain differences slightly fluctuate within ± 0.2 dBi at the low-frequency range (Fig. 4k), which is comparable to the previously reported work²¹. The performance can also be well maintained in the bent state with the bending radii of 1.5, 2.8, and 4.3 cm (Supplementary Fig. 20). The Ti_3C_2 antennas with the thickness of 3 and 10 μm also have similar results (Supplementary Figs. 21–24). Thus, the excellent cyclic bending stability of Ti_3C_2 antenna is well demonstrated for application in flexible RF devices. The actual communication performance of the Ti_3C_2 antenna is conducted using NI USPR-2943R platform. Two Ti_3C_2 antennas are connected to two antenna ports of the wireless communication platform through coaxial cables as transmitting and receiving antennas, respectively (Fig. 4l). The entire test process is real-time, using Binary Phase Shift Keying (BPSK) modulation technology. The upper left part of the computer monitor is the real-time transmission screen, the lower left part is the real-time receiving screen, and the right half is the communication status information, including the operating frequency, the distribution diagram of the signal vector endpoints (Planisphere) and the bit error rate diagram. The transmission performance of Ti_3C_2 antenna is tested by transmitting movie trailers through the wireless communication platform. When the antenna is flat, the point of the planisphere is very dense, meaning the high communication quality, and the bit error rate is almost zero (The left picture in Fig. 4l and Supplementary Movie 2). Currently, the transmitted movie is very clear. When the Ti_3C_2 antenna is bent horizontally or vertically, the points on the planisphere are slightly scattered, and the bit error rate at this time is still closed to zero, and the movie still transmits normally (The middle and right picture in Fig. 4l and Supplementary Movie 3). The detailed bending radii effects further indicate that the real-time movie transmission and reception of the Ti_3C_2 antennas can still be realized under the maximum bending angle ($>200^\circ$), demonstrating the advantages of mechanical flexibility (Supplementary Fig. 25 and Supplementary Movie 4). The transmission effect can also be achieved when the antennas are in the non-line of sight (Supplementary Fig. 26 and Supplementary Movie 5) or at different orientation angles (Supplementary Fig. 27 and Supplementary Movie 6). The real-time communication can also proceed in the long-range distance of 1–5 m (Supplementary Fig. 28 and Supplementary Movie 7). The communication between the antennas where one antenna transmits a signal generated by the signal generator and the receiving antenna reveals the response has been revealed in a spectrum analyzer (Supplementary Fig. 29). The specific real-time application of the flexible ultrawideband Ti_3C_2 monopole antennas is promising in various scenarios including human-computer interaction fields (i.e., smart medical treatment, individual combat, etc), IoT (i.e., real-time sensing, identity recognition, near-field communication, etc), mobile communication systems, large data transfer, video calls, multi-person online conferences, and information exchange of large data volumes. The humidity effect and heat effect on the antenna performance have been evaluated through the implementation of Ti_3C_2 antennas as radiating and sensing elements while the antenna sensor is connected to the

vector network analyzer, showing the sensing potentials in cutting-edge IoT applications (Supplementary Figs. 30 and 31).

Discussion

In summary, this work reports the elliptical ultrawideband Ti_3C_2 monopole antenna via high-resolution extrusion printing technology. The bandwidth of 1.7–4.0 GHz in the working frequency band covers WLAN, Bluetooth, and 5 G (n41, n78) frequency bands, which is comparable to the traditional Cu antenna and superior to previously reported Ti_3C_2 antennas. The molecular glue modification strategy realizes the compact conformal integration of Ti_3C_2 layer and F4B dielectric substrate in Ti_3C_2 antenna, which overcomes the non-resilience defects of traditional copper antenna. The S_{11} parameter and gain of Ti_3C_2 antennas are well maintained after 1000 bending cycles at the bending radii of 1.5, 2.8, and 4.3 cm. The excellent cyclic bending stability ensures fluent real-time wireless transmission for movie trailers in bending states, which is also the first demo instance of Ti_3C_2 antenna in recently reported works. This work presents a significant microelectronic printing technological advance in developing commercial antenna with excellent flexibility and ultrawideband for efficient wireless data communication and transmission at fast-growing IoT applications.

Methods

Materials

Ti_3AlC_2 powder (99.99 wt%) was purchased from II Technology Co., Ltd. LiF (99 wt%), dopamine hydrochloride (98 wt%) and tris-magnesium buffer (1 M, pH = 8.5) were purchased from Aladdin Biochemical Technology Co., Ltd. Hydrochloric acid (HCl) solution was purchased from Nanjing Chemical Reagent Co., Ltd. The dielectric substrate (F4B220M) was purchased from Shenzhen Dongxin Jiuzhou Technology Co., Ltd. All materials in this work were used as received without further purification.

Characterization

SEM image was characterized by scanning electron microscopy (FESEM, Hitachi S-4800). TEM image was measured by transmission electron microscopy (Hitachi HT7700). XRD pattern was carried out by X-ray diffractometer (Bruker AXS D8 Advance), using $\text{Cu K}\alpha$ radiation ($\lambda = 1.5406 \text{ \AA}$) over the range of $2\theta = 5.0 - 60.0^\circ$. FT-IR spectroscopy was obtained using FT-IR spectrophotometer (PerkinElmer Spectrum Two). XPS was performed on Thermo ESCALAB 250XI. Thin-film sheet resistance was tested by dual electric digital four-probe tester (ST2263, China). S_{11} and S_{21} of all TLs were measured by vector network analyzer (Rohde & Schwarz ZVA67). Radiation efficiency was measured in a SATIMO anechoic chamber. Signal transmission performance was carried out by the Universal Software Radio Peripheral (NI USRP-2943R). CST Microwave Studio, a full wave time domain finite integration method solver, was used to model Ti_3C_2 and copper microstrip TLs, and ultrawideband monopole antennas. In the actual measurement, Anritsu 3680k microwave test fixture was used instead of a pressed connector.

Preparation of m- Ti_3C_2 bulks

First, LiF (0.5 g) was dissolved in HCl (10 mL, 9 M). Then, the commercial Ti_3AlC_2 bulks (0.5 g) were slowly added to the mixture and conserved at 60°C for 24 h. Afterward, the products were washed with deionized water five times until the pH was above 6. Finally, the samples were dried under a vacuum for 12 h.

Preparation of Ti_3C_2 ink

m- Ti_3C_2 bulks (100 mg) were dispersed in 10 mL deionized water and sonicated (60 kHz, 360 W) for 1 h. Then, the dispersion was centrifuged at 3500 rpm for 1 h. 80% of the upper solution was sucked up to discard the unexfoliated m- Ti_3C_2 . Finally, the solution was

subsequently centrifuged at 5000 rpm for 1 h to collect the exfoliated Ti_3C_2 nanosheets.

Treatment of dielectric substrate

Ti_3C_2 microstrip TLs were designed with a characteristic impedance of 50Ω to transmit electromagnetic waves. The commercial F4BM220 dielectric substrate with a dielectric constant of 2.2 was chosen, in which the top copper-clad layer was etched away and the bottom copper-clad layer was retained. The dopamine hydrochloride (400 mg) was dissolved in deionized water (100 mL) and tris-magnesium buffer (30 mL) was diluted in deionized water (70 mL). The above solution was fully mixed in an open system, and the pH value was adjusted to 8.5 at 40°C . The pretreated dielectric substrate was immersed in the above mixture for 24 h under stirring. After the reaction was completed, the impurity on the surface was constantly washed away.

Design and simulation of Ti_3C_2 and copper TLs

Ti_3C_2 microstrip TLs are composed of three layers, including the dielectric layer (F4BM220), the conductor Ti_3C_2 layer, and the ground plane (copper). Ti_3C_2 TL with 0.8 mm width and 30 mm length was designed for testing. The pressed connector was modelled with a wave port excitation. In order to minimize the reflection coefficient, a copper microstrip TL with a width of 0.8 mm and a thickness of $18 \mu\text{m}$ was designed to match the system characteristic impedance of 50Ω . In the testing scenario, the electromagnetic waves ranged from 1 to 10 GHz. Copper microstrip TL was fabricated externally by manufacturers using standard printed circuit boards fabrication process.

Ti_3C_2 microstrip TLs measurement

Anritsu 3680k microwave test fixture was used for the interconnection between Ti_3C_2 TL and vector network analyzer cable. Scattering parameters of TL were measured using a vector network analyzer (Rohde & Schwarz ZVA67). The attenuation constant (α) of Ti_3C_2 microstrip TL with the length of 30 mm was evaluated based on the S-parameters. The Eq. (1) was as follows.

$$\alpha = \frac{1}{l} 10 \lg \left(\frac{1 - |S_{11}|^2}{|S_{21}|^2} \right) \quad (1)$$

where l (mm) is the length of TL, S_{11} is reflection coefficient, and S_{21} is transmission coefficient.

Design and simulation of ultrawideband monopole antenna

Ti_3C_2 antennas and Cu antennas were modeled by considering the skin depth, surface roughness and conductivity of the conductor. The specific size of the elliptical ultrawideband monopole antenna was determined by the following Eqs. (2) and (3)⁴⁸.

$$f_L = \frac{7.2}{[(L+r+p) \times k]} \quad (2)$$

$$2 \times \pi \times r \times L = \pi \times a \times b \quad (3)$$

Where k is taken as 0.823 empirically for a dielectric layer with $\epsilon_r = 2.2$ and $h = 0.254 \text{ mm}$. L is the long axis of the ellipse, $b = L/2$, and r is the effective radius of an equivalent cylindrical monopole antenna. p is the length of the 50Ω feed line when the TL width is 0.8 mm. We first assume that $L = 3.9 \text{ cm}$, $p = 0.1 \text{ cm}$, and $r \approx 0.375 \text{ cm}$ can be determined by Eq. (2). Then, the value of $a \approx 1.5 \text{ cm}$ can be determined by Eq. (3).

By adjusting the axial ratio of the ellipse and the design of the ground plane, the bandwidth of the antenna can be increased. The antenna was simulated using a time domain solver. The 3D radiation pattern of Ti_3C_2 antenna was also drawn using CST as shown in Supplementary Fig. 18. As the frequency increases, 3D pattern of the

antennas had no obvious changes, maintaining an omnidirectional radiation state.

Antenna measurement

Radiation efficiency measurement. It was performed in a SATIMO anechoic chamber.

Gain measurement. It was performed in a far-field anechoic chamber. The accurate gain of ultrawideband Ti_3C_2 monopole antennas in a far-field anechoic chamber was measured using gain-transfer (gain-comparison) method⁴⁹. The transmitting antenna and the receiving antenna facing each other at the same height were separated by a certain distance. The standard transmitting antenna in this experiment was a log-periodic antenna for 0.5–6 GHz (A-INFO DS-50600, Chengdu, China). The receiving antennas in this experiment included two parts. One part of receiving antennas consisted of standard gain horn antennas of 1.7–2.6 GHz, 2.6–3.95 GHz, and 3.95–5.85 GHz (A-INFO LB-430-10, LB-284-10, and LB-187-15, Chengdu, China). The gain (G_{REF}) of a standard gain horn antenna was known from the antenna manual provided by antenna manufacturers. The other part of receiving antennas consisted of a Ti_3C_2 antenna (i.e., Ti_3C_2 -3 μm , Ti_3C_2 -5.5 μm , and Ti_3C_2 -10 μm) and a copper antenna. A laser level was used to calibrate the height of the transmitting and receiving antennas. The antenna test software (AT Studio) that matched with the far-field anechoic chamber was used to measure the realized gain.

The transmitting frame and receiving a frame of the antenna were shown in Supplementary Fig. 13, and the receiving frame can be rotated 360° around the Z axis. The transmitting antenna was set up and excited with a power of 10 dBm. The receiving electrical level (E_{REF}) of the horizontal polarization direction and the vertical polarization direction of the standard gain horn antenna were tested first. Then the receiving electrical level (E_{AUT}) of the horizontal polarization direction and the vertical polarization direction of a Ti_3C_2 antenna (i.e., Ti_3C_2 -3 μm , Ti_3C_2 -5.5 μm and Ti_3C_2 -10 μm) and a copper antenna were tested. Finally, the realized gain of the Ti_3C_2 antenna was calculated by the following Eq. (4).

$$G_{\text{AUT}} = (E_{\text{AUT}} - E_{\text{REF}}) + G_{\text{REF}} \quad (4)$$

Radiation pattern measurement. It was performed in a far-field anechoic chamber. The radiation pattern of Ti_3C_2 antenna was measured in the far-field anechoic chamber. The system can scan 360° of the antenna. For scanning, it is necessary to ensure that the transmitting and receiving antennas maintained the same polarization direction. The normalized radiation pattern can be obtained by simply processing the measured radiation pattern. Data was recorded by 0.1° sweeping azimuth (φ) and 0.1° sweeping roll (θ).

Humidity effect measurement. The humidity effect on the antenna performance has been evaluated through the implementation of Ti_3C_2 antenna as radiating and sensing element while the antenna sensor is connected to the vector network analyzer (Supplementary Fig. S30a). The antenna sensor is positioned inside the sealed custom-made chamber, and the humidity is pumped by the humidifier. The resonant peak is used as the initial frequency to measure the resonant frequency shift during humidity sensing measurement (Supplementary Fig. S30b,c).

Heat effect measurement. The heat effect on the antenna performance has been measured through the implementation of Ti_3C_2 antenna as radiating and sensing elements while the antenna sensor is connected to the vector network analyzer (Supplementary Fig. S31a). The antenna is irradiated by an infrared lamp (317 mW cm^{-2}) as a heat source, and the thermal imager is used to monitor the real-time temperature (Supplementary Fig. S31b).

Data availability

The datasets generated during and/or analyzed during the current study are available from the corresponding author on reasonable request. Source data are provided with this paper.

References

- Papadopoulos, N. et al. Touchscreen tags based on thin-film electronics for the internet of everything. *Nat. Electron.* **2**, 606–611 (2019).
- Shao, Y. et al. Room-temperature high-precision printing of flexible wireless electronics based on MXene inks. *Nat. Commun.* **13**, 3223 (2022).
- Kimionis, J., Georgiadis, A., Daskalakis, S. N. & Tentzeris, M. M. A printed millimetre-wave modulator and antenna array for backscatter communications at gigabit data rates. *Nat. Electron.* **4**, 439–446 (2021).
- Pan, K. et al. Sustainable production of highly conductive multilayer graphene ink for wireless connectivity and IOT applications. *Nat. Commun.* **9**, 5197 (2018).
- Martin, A., Chang, B. S., Pauls, A. M., Du, C. & Thuo, M. Stabilization of undercooled metals via passivating oxide layers. *Angew. Chem. Int. Ed.* **60**, 5928–5935 (2021).
- Lv, S. et al. Reactive inkjet printing of graphene based flexible circuits and radio frequency antennas. *J. Mater. Chem. C.* **9**, 13182–13192 (2021).
- Thanh Tung, T., Chen, S. J., Fumeaux, C., Kim, T. & Losic, D. N-doped reduced graphene oxide-PEDOT nanocomposites for implementation of a flexible wideband antenna for wearable wireless communication applications. *Nanotechnology* **32**, 245711 (2021).
- Sarycheva, A. et al. 2D titanium carbide (MXene) for wireless communication. *Sci. Adv.* **4**, eaau0920 (2018).
- VahidMohammadi, A., Rosen, J. & Gogotsi, Y. The world of two-dimensional carbides and nitrides (MXenes). *Science* **372**, eabf1581 (2021).
- Khorsand Kazemi, K. et al. MXene membrane in planar microwave resonant structures for 5G applications. *Appl. Mater. Today* **26**, 101294 (2022).
- Khorsand Kazemi, K. et al. Low-profile planar antenna sensor based on $\text{Ti}_3\text{C}_2\text{T}_x$ MXene membrane for VOC and humidity monitoring. *Adv. Mater. Interfaces* **9**, 2102411 (2022).
- Zhao, W. et al. Ultrathin Ti_3C_2 nanowires derived from multi-layered bulks for high-performance hydrogen evolution reaction. *Chin. Chem. Lett.* **33**, 557–561 (2022).
- Zhang, Y. Z. et al. MXene printing and patterned coating for device applications. *Adv. Mater.* **32**, 1908486 (2020).
- Yu, L. et al. Versatile N-doped MXene ink for printed electrochemical energy storage application. *Adv. Energy Mater.* **9**, 1901839 (2019).
- Scholz, A. et al. Hybrid low-voltage physical unclonable function based on inkjet-printed metal-oxide transistors. *Nat. Commun.* **11**, 5543 (2020).
- Hassan, K. et al. Functional inks and extrusion-based 3D printing of 2D materials: a review of current research and applications. *Nanoscale* **12**, 19007–19042 (2020).
- Hu, G. et al. A general ink formulation of 2D crystals for wafer-scale inkjet printing. *Sci. Adv.* **6**, eaba5029 (2020).
- Hassan, K. et al. Extrusion-printed CNT-graphene sensor array with embedded MXene/PEDOT:PSS heater for enhanced NO_2 sensing at low temperature. *Adv. Mater. Interfaces* **8**, 2101175 (2021).
- Lamminen, A. et al. Graphene-flakes printed wideband elliptical dipole antenna for low-cost wireless communications applications. *IEEE Antennas Wirel. Propag. Lett.* **16**, 1883–1886 (2017).
- Hong, S., Kim, Y. & Jung, C. W. Transparent microstrip patch antennas with multilayer and metal-mesh films. *IEEE Antennas Wirel. Propag. Lett.* **16**, 772–775 (2017).

21. Han, M. et al. Solution-processed $\text{Ti}_3\text{C}_2\text{T}_x$ MXene antennas for radio-frequency communication. *Adv. Mater.* **33**, 2003225 (2021).
22. Wen, D. et al. Inkjet printing transparent and conductive MXene ($\text{Ti}_3\text{C}_2\text{T}_x$) films: a strategy for flexible energy storage devices. *ACS Appl. Mater. Interfaces* **13**, 17766–17780 (2021).
23. Piatti, E. et al. Charge transport mechanisms in inkjet-printed thin-film transistors based on two-dimensional materials. *Nat. Electron.* **4**, 893–905 (2021).
24. Gao, L. et al. Applications of few-layer Nb_2C MXene: narrow-band photodetectors and femtosecond mode-locked fiber lasers. *ACS Nano* **15**, 954–965 (2021).
25. Zheng, S. et al. Multitasking MXene inks enable high-performance printable microelectrochemical energy storage devices for all-flexible self-powered integrated systems. *Adv. Mater.* **33**, 2005449 (2021).
26. Ma, Y. et al. A highly flexible and sensitive piezoresistive sensor based on MXene with greatly changed interlayer distances. *Nat. Commun.* **8**, 1207 (2017).
27. Hu, X. et al. Understanding the self-polymerization mechanism of dopamine by molecular simulation and applying dopamine surface modification to improve the interfacial adhesion of polyimide fibers with epoxy resin matrix. *High. Perform. Polym.* **33**, 601–614 (2021).
28. Yan, R. T. et al. A broadband and high-efficiency compact transition from microstrip line to spoof surface plasmon polaritons. *IEEE Microw. Wirel. Compon. Lett.* **30**, 23–26 (2020).
29. Kuang, J., Guo, J. L. & Messersmith, P. B. High ionic strength formation of DOPA-melanin coating for loading and release of cationic antimicrobial compounds. *Adv. Mater. Interfaces* **1**, 1400145 (2014).
30. Lee, H. A., Ma, Y., Zhou, F., Hong, S. & Lee, H. Material-independent surface chemistry beyond polydopamine coating. *Acc. Chem. Res.* **52**, 704–713 (2019).
31. Li, T. et al. Sandwich-structured ordered mesoporous polydopamine/MXene hybrids as high-performance anodes for lithium-ion batteries. *ACS Appl. Mater. Interfaces* **12**, 14993–15001 (2020).
32. Rodenstein, M., Zürcher, S., Tosatti, S. G. P. & Spencer, N. D. Fabricating chemical gradients on oxide surfaces by means of fluorinated, catechol-based, self-assembled monolayers. *Langmuir* **26**, 16211–16220 (2010).
33. Saiz-Poseu, J., Mancebo-Aracil, J., Nador, F., Busqué, F. & Ruiz-Molina, D. The chemistry behind catechol-based adhesion. *Angew. Chem. Int. Ed.* **58**, 696–714 (2019).
34. Zangmeister, R. A., Morris, T. A. & Tarlov, M. J. Characterization of polydopamine thin films deposited at short times by autoxidation of dopamine. *Langmuir* **29**, 8619–8628 (2013).
35. Syres, K., Thomas, A., Bondino, F., Malvestuto, M. & Grätzel, M. Dopamine adsorption on anatase $\text{TiO}_2(101)$: a photoemission and NEXAFs spectroscopy study. *Langmuir* **26**, 14548–14555 (2010).
36. Rodríguez, R., Blesa, M. A. & Regazzoni, A. E. Surface complexation at the $\text{TiO}_2(\text{anatase})/\text{aqueous solution}$ interface: chemisorption of catechol. *J. Colloid Interface Sci.* **177**, 122–131 (1996).
37. Lee, G. S. et al. Mussel inspired highly aligned $\text{Ti}_3\text{C}_2\text{T}_x$ MXene film with synergistic enhancement of mechanical strength and ambient stability. *ACS Nano* **14**, 11722–11732 (2020).
38. Abdolhosseinzadeh, S., Jiang, X., Zhang, H., Qiu, J. & Zhang, C. Perspectives on solution processing of two-dimensional MXenes. *Mater. Today* **48**, 214–240 (2021).
39. Hu, G. et al. Black phosphorus ink formulation for inkjet printing of optoelectronics and photonics. *Nat. Commun.* **8**, 278 (2017).
40. Yang, W. et al. 3D printing of freestanding MXene architectures for current-collector-free supercapacitors. *Adv. Mater.* **31**, 1902725 (2019).
41. Akuzum, B. et al. Rheological characteristics of 2D titanium carbide (MXene) dispersions: A guide for processing MXenes. *ACS Nano* **12**, 2685–2694 (2018).
42. Lu, Q., Zhu, Z., Liu, Y., Liu, X. & Yin, X. Wideband electromagnetic modeling of coaxial-annular through-silicon vias. *IEEE Trans. Electromagn. Compat.* **60**, 1915–1922 (2018).
43. Li, Y. et al. Reversible crumpling of 2D titanium carbide (MXene) nanocoatings for stretchable electromagnetic shielding and wearable wireless communication. *Adv. Funct. Mater.* **30**, 1907451 (2020).
44. Belohoubek, E. & Denlinger, E. Loss considerations for microstrip resonators. *IEEE Trans. Microw. Theory Tech.* **23**, 522–526 (1975).
45. Yang, Z. J., Zhu, L. & Xiao, S. An implantable circularly polarized patch antenna design for pacemaker monitoring based on quality factor analysis. *IEEE Trans. Antennas Propag.* **66**, 5180–5192 (2018).
46. Kraus, J. D. & Marhefka, R. J. *Antenna: For All Applications (Third Editions)* (Publishing House of Electronics Industry, Beijing, 2011).
47. Xu, K. et al. A printed single-layer UWB monopole antenna with extended ground plane stubs. *IEEE Antennas Wirel. Propag. Lett.* **12**, 237–240 (2013).
48. Liang, J., Chiau, C. C., Chen, C. & Parini, C. G. Study of a printed circular disc monopole antenna for UWB systems. *IEEE Trans. Antennas Propag.* **53**, 3500–3504 (2005).
49. Balanis, C. A. *Antenna theory: Analysis and design* (John Wiley & Sons, 2015).

Acknowledgements

This work was supported by National Funds for Distinguished Young Scientists (61825503 (Q.Z.)), National Natural Science Foundation of China (62174086 (W.Z.), 62001250 (L.L.), 62288102 (W.H.), and 61772287 (F.T.)), and Postgraduate Research & Practice Innovation Program of Jiangsu Province (SJCX22_0253 (F.L.)).

Author contributions

W.Z. and H.N. contributed equally to this work. L.L., W.H., and Q.Z. conceived the idea and supervised the project. W.Z. designed the project and wrote the manuscript. H.N. co-wrote the manuscript and performed the device measurement. C.D. carried out the device fabrication and characterization. F.Q., F.L., F.T., and P.Y. performed ink development and characterization experiments. S.L., W.He., and X.W. performed materials synthesis. All authors contributed to analyze the data.

Competing interests

The authors declare no competing interests.

Additional information

Supplementary information The online version contains supplementary material available at <https://doi.org/10.1038/s41467-022-35371-6>.

Correspondence and requests for materials should be addressed to Leilei Liu, Wei Huang or Qiang Zhao.

Peer review information *Nature Communications* thanks Mohammad Zarifi, and the other, anonymous, reviewers for their contribution to the peer review of this work. Peer reviewer reports are available.

Reprints and permissions information is available at <http://www.nature.com/reprints>

Publisher's note Springer Nature remains neutral with regard to jurisdictional claims in published maps and institutional affiliations.

Open Access This article is licensed under a Creative Commons Attribution 4.0 International License, which permits use, sharing, adaptation, distribution and reproduction in any medium or format, as long as you give appropriate credit to the original author(s) and the source, provide a link to the Creative Commons license, and indicate if changes were made. The images or other third party material in this article are included in the article's Creative Commons license, unless indicated otherwise in a credit line to the material. If material is not included in the article's Creative Commons license and your intended use is not permitted by statutory regulation or exceeds the permitted use, you will need to obtain permission directly from the copyright holder. To view a copy of this license, visit <http://creativecommons.org/licenses/by/4.0/>.

© The Author(s) 2023